CHEMISTRY OF MATERIALS

Article

pubs.acs.org/cm

The Intercalation Phase Diagram of Mg in V_2O_5 from First-Principles

Gopalakrishnan Sai Gautam, Pieremanuele Canepa, Aziz Abdellahi, Alexander Urban, Rahul Malik, and Gerbrand Ceder*

Department of Materials Science and Engineering, Massachusetts Institute of Technology, Cambridge, Massachusetts 02139, United States

ABSTRACT: We have investigated Mg intercalation into orthorhombic V_2O_5, one of only three cathodes known to reversibly intercalate Mg ions. By calculating the ground-state $Mg_xV_2O_5$ configurations and by developing a cluster expansion for the configurational disorder in δ-V_2O_5, a full temperature−composition phase diagram is derived. Our calculations indicate an equilibrium phase-separating behavior between fully demagnesiated α-V_2O_5 and fully magnesiated δ-V_2O_5, but also motivate the existence of potentially metastable solid solution transformation paths in both phases. We find significantly better mobility for Mg in the δ polymorph, suggesting that better performance can be achieved by cycling Mg in the δ phase.

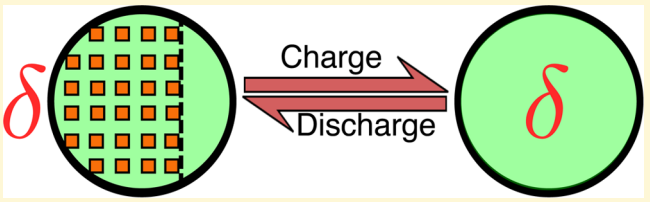

1. INTRODUCTION

A multivalent (MV) battery chemistry, which pairs a non-dendrite forming Mg metal anode with a high voltage (~3 V) intercalation cathode, offers a potentially safe and inexpensive high-energy-density storage system with the potential to outperform current Li-ion technology.[1] A change in chemistry leads to new challenges, however, one being the design of a cathode that can reversibly intercalate Mg at a high enough voltage. Orthorhombic V_2O_5 is one such material that offers exciting prospects of being a reversible intercalating cathode for Mg batteries.[2−4] The theoretical energy density of a cathode based on Mg intercalation into V_2O_5 is ~660 Wh/kg,[5] which approaches the practical energy densities of current commercial Li-ion chemistries (~700 Wh/kg for $LiCoO_2$[6]), but the major benefit of switching to a MV chemistry is the gain in volumetric energy density arising from the usage of a metallic anode (~3833 mAh/cm^3 for Mg,[2] compared to ~800 mAh/cm^3 for Li insertion into graphite[5]).

The orthorhombic V_2O_5 structure has been well-characterized, because of its interesting spin ladder characteristics and widely known Li intercalation properties, with a reversible capacity of ~130 mAh/g and voltage of ~3.3 V vs Li metal.[7−13] Consequently, Li intercalation into V_2O_5 has been the subject of several experimental[14−18] and theoretical[19−21] studies. Li−V_2O_5 undergoes several first-order phase transformations during intercalation, such as the $\alpha \rightarrow \epsilon$ and $\epsilon \rightarrow \delta$ between x_{Li} = 0 and x_{Li} = 1, the irreversible $\delta \rightarrow \gamma$ transition at x_{Li} >1, and another irreversible $\gamma \rightarrow \omega$ transition at x_{Li} > 2.[14] Several authors have investigated Mg-insertion into V_2O_5[13,22−25] and, to date, V_2O_5 is one of only three cathode materials to have shown reversible intercalation of Mg, the other two being the chevrel Mo_3S_4[3] and layered MoO_3.[25]

While Li-ion has been investigated extensively for the past ~25 years, there are significantly fewer studies, theoretical or otherwise, of Mg intercalation hosts in the literature. Pereira-Ramos et al.[22] showed electrochemical intercalation of Mg into V_2O_5 (at 150 °C and 100 μA/cm^2 current density), and Gregory et al.[23] have reported chemical insertion of Mg up to $Mg_{0.66}V_2O_5$. Novak et al.[26] demonstrated reversible electrochemical insertion of Mg in V_2O_5 at room temperature while also demonstrating superior capacities (~170 mAh/g) using an acetonitrile (AN) electrolyte containing water as opposed to dry AN. Yu et al.[27] showed similar improvements in capacity (~158.6 mAh/g) using a H_2O + polycarbonate (PC) system, compared to dry PC. Electrochemical insertion of Mg into V_2O_5 nanopowders and thin films using activated carbon as the counter electrode was shown by Amatucci et al.[13] and Gershinsky et al.,[25] respectively, and insertion into V_2O_5 single crystals was reported by Shklover et al.[28]

Thus far, all reported experimental attempts have begun in the charged state and succeeded in reversibly inserting only about half a Mg ($x_{Mg} \approx 0.5$) per formula unit of V_2O_5, in contrast to Li−V_2O_5, where up to $x_{Li} \approx 3$ has been inserted per V_2O_5.[14,22,27,28] When the grain size of V_2O_5 is reduced, e.g., nanopowders and thin films, insertion levels can reach $x_{Mg} \approx 0.6$.[13,25] In addition, in cells where a Mg metal anode was used, rapid capacity fade was reported upon cycling.[26,27] Unlike Li intercalation systems, anode passivation by the electrolytes is a major issue for Mg batteries using a Mg metal anode.[27] Out of the two experiments that have not reported significant capacity fade so far,[13,25] the work done by Gershinsky et al. is particularly useful to benchmark theoretical models, because the Mg insertion was done at extremely low rates (0.5 μA/cm^2), and therefore corresponds most to equilibrium conditions.

Previous theoretical studies of the Mg−V_2O_5 system have benchmarked structural parameters, average voltages, and the electronic properties of layered V_2O_5 upon Mg insertion.[29−31]

Received: March 13, 2015
Revised: April 28, 2015
Published: April 28, 2015

DOI: 10.1021/acs.chemmater.5b00957
Chem. Mater. 2015, 27, 3733−3742

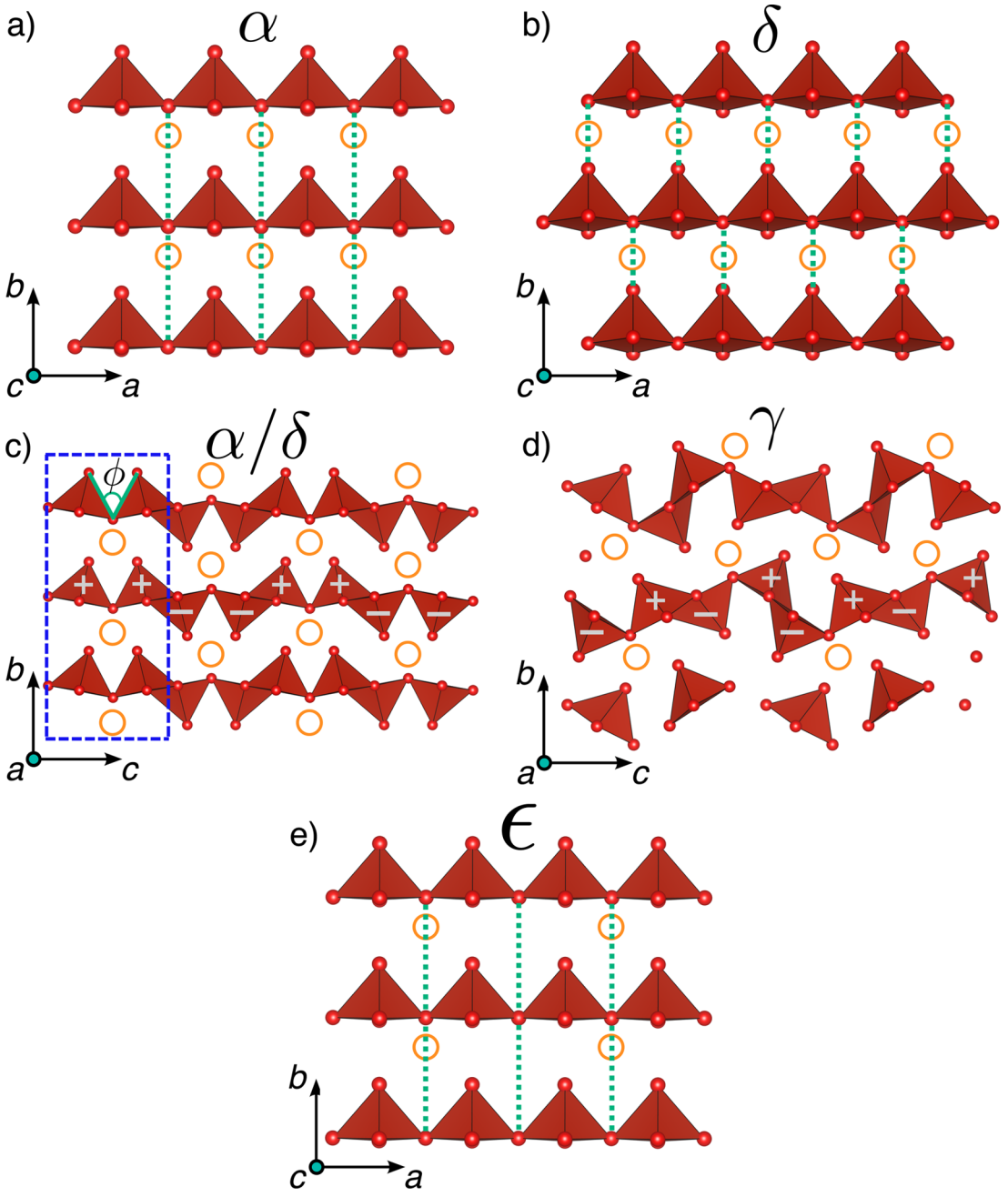

Figure 1. (a) α and (b) δ polymorphs of orthorhombic V_2O_5 are shown along the c-axis (shown to a depth of $c/2$ for viewing clarity) and (c) along the a-axis, which, compared to the (d) γ polymorph, has a different orientation of VO_5 pyramids as denoted by the "+" and "−" symbols along the c-axis. Hollow orange circles correspond to the intercalation sites, the green dotted lines show the differences in layer stacking, and the dashed blue rectangle in panel (c) indicates a distance of $c/2$. Panel (e) illustrates the ϵ phase corresponding to a specific ordering of Mg atoms in α-V_2O_5 at half magnesiation, where alternate intercalant sites are occupied in the a-axis, as indicated by the orange circles. The schematics here correspond to "supercells" of the respective polymorph unit cells.

Wang et al.[29] showed an increase in the Mg binding energy and Li mobility in single-layered V_2O_5 compared to bulk V_2O_5. Carrasco[30] found that, although incorporating van der Waals dispersion corrections in the calculations improved the agreement of the lattice parameters with experiments, it led to an overestimation of the voltage. Zhou et al.[31] calculated the band structures, average voltages, Mg migration barriers, and the $\alpha \rightarrow \delta$ phase transformation barrier in Mg–V_2O_5. While reporting higher computed average voltage for Mg–V_2O_5, compared to the Li–V_2O_5 system (in apparent disagreement with experiments[14,25]), the authors explained the slow diffusion of Mg in V_2O_5 by predicting a facile $\alpha \rightarrow \delta$ transition coupled with an estimated lower Mg mobility in δ than α.[31]

In the present work, we have explored in detail the physics of room temperature Mg intercalation in orthorhombic V_2O_5 using first-principles calculations. Compared to Li, Mg insertion is accompanied by twice the number of electrons, which means that the properties of the Mg intercalation system will be largely dictated by how the additional electron localizes on the nearby V atoms. To study the combined effects not only of inserting a different ion but also a different number of electrons on the equilibrium phase behavior, we calculate the Mg–V_2O_5

DOI: 10.1021/acs.chemmater.5b00957
Chem. Mater. 2015, 27, 3733−3742

intercalation phase diagram using the cluster expansion-Monte Carlo approach. A similar approach has been previously used to study Li-intercalation systems[32,33] and can be derived formally through systematic coarse-graining of the partition function.[34] Our calculations focus particularly on Mg intercalation into the α and δ polymorphs of V_2O_5, evaluating their respective ground state hulls, subsequent voltage curves, and activation barriers for Mg diffusion. We have also constructed the temperature−composition phase diagram for Mg in the δ polymorph.

2. POLYMORPHS OF V_2O_5

The V_2O_5 structure consists of layers of VO_5 pyramids, each of which have 4 V−O bonds that form the base of the pyramid and one V═O (Vanadyl) bond that forms the apex. Each layer consists of alternate corner- and edge-sharing pyramids, with an offset in the *a*-axis between the edge-sharing pyramids. The different polymorphs of V_2O_5 observed experimentally are illustrated in Figure 1,[14] with the α (space group *Pmmn*), δ (*Cmcm*), and γ (*Pnma*) polymorphs all having orthorhombic symmetry. The notation, specific to this work, is *a* being the shortest axis of the lattice (3.56 Å for α; 3.69 Å for δ), *b* being the axis perpendicular to the layers indicative of the layer spacing (4.37 Å; 9.97 Å), and *c* being the longest axis (11.51 Å; 11.02 Å). Pure V_2O_5 crystallizes in the α phase at 298 K and remains stable at higher temperatures,[14] while the fully magnesiated phase (MgV_2O_5) has been found to form in the structure of the δ polymorph.[35] For simpler visualization, a single slice of the α and δ polymorphs, corresponding to a depth of $c/2$ (illustrated by the dashed blue rectangle in Figure 1c) is shown in Figures 1a and 1b, respectively. The α and δ polymorphs are very similar when viewed along the *a*-axis or the *b*−*c* plane (Figure 1c).

The main difference between the δ phase and the α phase is a translation of alternating V_2O_5 layers in the *a*-direction by "*a*/2", which doubles the "*b*" lattice parameter (as well as the unit cell) of the δ phase. The Mg sites in both α and δ are situated near the middle of the VO_5 pyramids (along *a*) and between the 2 layers (along *b*), as illustrated by the orange circles in Figure 1. As a result of shifting of layers between the α and δ phases, the anion coordination environment of the Mg sites also changes. Considering a Mg−O bond length cutoff of 2.5 Å, the Mg in the α phase is 8-fold coordinated (4 nearest neighbor O atoms and 4 next-nearest neighbors, 4 + 4) whereas the Mg in the δ phase is 6-fold coordinated (4 + 2). In this work, the ϵ phase is a specific ordering of Mg atoms on the α-V_2O_5 host at half magnesiation, as shown in Figure 1e. This intercalant ordering is observed in the Li−V_2O_5 system,[14] and has intercalant ions at alternate sites along the *a*-axis, as illustrated by the absence of Mg sites in Figure 1e.[20,36] The VO_5 pyramids in the α and δ phases "pucker" upon Li intercalation, as observed experimentally by Cava et al.[37] For the sake of simplicity, we define puckering here as the angle ϕ, as shown in Figure 1c. As the pyramids pucker with intercalation, ϕ decreases.

In the Li−V_2O_5 system, at x_{Li} >1, the host structure undergoes an irreversible phase transformation to form the γ phase, in which the VO_5 pyramids adopt a different orientation compared to α and δ, as seen in Figures 1c and 1d.[14] In the γ phase, the VO_5 pyramids along the *c*-direction alternate between up and down (denoted by the symbols "+" and "−" in Figure 1); whereas, in α and δ, the sequence is "up−up−down−down" (++−−). The γ phase has not yet been reported in the Mg−V_2O_5 system and hence will not be further discussed in this paper.

3. METHODOLOGY

To compute the ground-state hull and the average open circuit voltage curves we use Density Functional Theory (DFT), as implemented in VASP with the Perdew−Burke−Ernzerhof (PBE) exchange-correlation functional.[38−41] The Projector Augmented Wave theory,[42] together with a well-converged energy cutoff of 520 eV, is used to describe the wave functions, which are sampled on a Γ-centered 4 × 4 × 4 *k*-point mesh. In order to remove the spurious self-interaction of the vanadium *d*-electrons, a Hubbard *U* correction of 3.1 eV is added to the Generalized Gradient Approximation (GGA) Hamiltonian (GGA+*U*),[43,44] as fitted by Jain et al.[45] All Mg−V_2O_5 structures are fully relaxed within 0.25 meV/f.u.

To obtain the temperature−composition phase diagram, Grand canonical Monte Carlo (GMC) simulations are performed on a cluster expansion (CE) Hamiltonian. The CE is a parametrization of the total energy with respect to the occupancy of a predefined topology of sites, which, in this case, are the possible Mg insertion sites.[34,46,47] In practice, the CE is written as a truncated summation of the Effective Cluster Interactions (ECIs) of the pair, triplet, quadruplet, and higher-order terms, as given in eq 1.

$$E(\sigma) = \sum_{\alpha} m_{\alpha} V_{\alpha} \langle \prod_{i \in \beta} \sigma_i \rangle \tag{1}$$

where the energy (E) of a given configuration of Mg ions (σ) is obtained as a summation over all symmetrically distinct clusters (α). Each term in the sum is a product of the multiplicity *m*, the effective cluster interaction (ECI) *V* for a given α, and the occupation variable σ_i averaged over all clusters β that are symmetrically equivalent to α in the primitive cell of the given lattice. In this work, the CE is performed on the Mg sublattice and the various configurations correspond to the arrangement of Mg ($\sigma_i = 1$) and vacancies (Va; $\sigma_i = -1$) on the available Mg sites. The Pymatgen library is used to generate the various Mg-Va arrangements to be calculated with DFT.[48−51] The CE is built on the DFT formation energy of 97 distinct Mg-Va configurations using the compressive sensing paradigm and optimized through the split-Bregman algorithm.[52,53] The root-mean-square error (RMSE) and the weighted cross-validation (WCV) score are used to judge the quality and the predictive ability of the fit, respectively.[54]

The high-temperature phase diagram is then obtained with GMC calculations on supercells containing at least 1728 Mg/Va sites (equivalent to a 12 × 6 × 6 supercell of the conventional unit cell) and for a minimum of 100 000 equilibration steps followed by 200 000 sampling steps.[55] Monte Carlo scans are done on a range of chemical potentials at different temperatures, and phase transitions are detected by discontinuities in Mg concentration and energies. In order to remove numerical hysteresis from the Monte Carlo simulations, particularly at low temperatures, free energy integration is performed[56] with the fully magnesiated and fully demagnesiated phases as reference states.

Finally, the activation barriers associated with Mg diffusion in V_2O_5 are calculated with DFT, using the Nudged Elastic Band method (NEB)[57] and forces converged within 100 meV/Å. A minimum distance of 9 Å is introduced between the diffusing species and nine distinct images are used to capture the

DOI: 10.1021/acs.chemmater.5b00957
Chem. Mater. 2015, 27, 3733−3742

diffusion trajectory. As previously indicated by Liu et al.,[58] the convergence of GGA+U NEB calculations is problematic; hence, standard GGA is used to compute the Mg diffusion barriers.

4. RESULTS

4.1. Mg−V_2O_5 Ground State Hull. Figure 2 shows the ground-state hull and average voltage curves as a function of

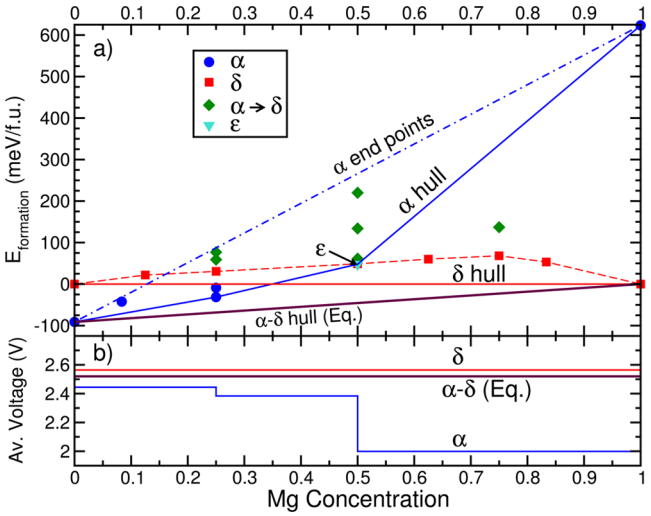

Figure 2. (a) The ground-state hull of Mg in V_2O_5 considering both α and δ phases. The formation energy per formula unit has been plotted with respect to Mg concentration. (b) The average voltage curves at 0 K for the α and δ phases with respect to pure Mg metal, obtained from the respective hulls are plotted against the Mg concentration.

Mg concentration in V_2O_5, as computed by DFT. The solid blue and red lines in Figure 2a indicate the ground-state hulls of the α and δ polymorphs, respectively. All formation energies are referenced to the fully magnesiated and fully demagnesiated end points of the δ-phase. The overall equilibrium behavior of the system is that of phase separation between unintercalated α-V_2O_5 and fully intercalated δ-$Mg_1V_2O_5$, as indicated by the solid maroon line. As can be observed, the α phase is stable, compared to the δ phase at low Mg concentrations up to $x_{Mg} \approx 0.35$, where the α and δ hulls intersect, and the δ phase is stable at higher Mg concentrations. In Figure 2a, the dash-dotted blue line indicates the end members of the α hull (pure α-V_2O_5 and α-$Mg_1V_2O_5$), and the dashed red line represents the lowest energy configurations computed at intermediate Mg concentrations for the δ phase.

The α-hull represents the energy trajectory for metastable Mg insertion into α-V_2O_5 (i.e., without transformation of the host to δ), and it displays a convex shape with ground-state configurations at Mg concentrations of 0.25 and 0.5. The most stable configuration at $x_{Mg} = 0.5$ in the α hull is the ϵ phase. In contrast, there are no metastable Mg orderings in the δ phase, implying that, in the δ-phase host, the Mg ions will want to phase separate into MgV_2O_5 and V_2O_5 domains. Some Mg configurations when initialized in the α phase relax to the δ phase, as indicated by the green diamond points in Figure 2a. These structures undergo a shear-like transformation from α to δ, which involves V_2O_5 layers sliding along the a-direction. This mechanical instability phenomenon has been observed in our calculations both at low Mg concentrations ($x_{Mg} = 0.25$) and at high Mg concentrations ($x_{Mg} = 0.75$), but never at very low Mg concentrations ($x_{Mg} = 0.08$).

The Mg insertion voltage will be dependent on which of the possible stable or metastable paths the system follows and the voltage for several possible scenarios is shown in Figure 2b. The equilibrium voltage curve is a single plateau at 2.52 V vs Mg metal, consistent with phase-separating behavior between α-V_2O_5 and δ-$Mg_1V_2O_5$. The voltage for the metastable insertion in the α host averages ~2.27 V vs Mg metal for $0 < x_{Mg} < 1$ and exhibits a steep potential drop of ~400 mV at $x_{Mg} = 0.5$, corresponding to the ϵ ordering. Metastable Mg insertion in δ occurs on a single plateau at 2.56 V vs Mg metal, consistent with phase separation between δ-$Mg_0V_2O_5$ and fully intercalated δ-$Mg_1V_2O_5$. The average voltage of the α phase best agrees with the experimental average voltage of ~2.3 V.[13,25]

4.2. Puckering and Layer Spacing. The VO_5 pyramids in both α and δ-V_2O_5 pucker upon Mg intercalation, quantified by the angle ϕ shown in Figure 1c. We find that ϕ decreases (corresponding to increased puckering) with increasing Mg concentration, resulting in the formation of ripples in the layers. Current calculations show a decrease from $\phi \approx 76°$ at $x_{Mg} = 0$ (which corresponds to flat layers) to $\phi \approx 56°$ at $x_{Mg} = 1$ in the α phase and a decrease from $\phi \approx 68°$ at $x_{Mg} = 0$ to $\phi \approx 54°$ at $x_{Mg} = 1$ in δ-V_2O_5.

Figure 3 shows the variation of the V_2O_5 layer spacing (seen in Figures 1a and 1b), as a function of Mg concentration in

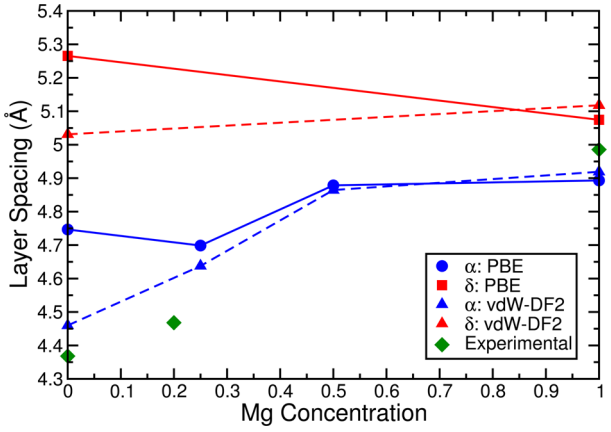

Figure 3. Variation of layer spacing with Mg concentration in both α and δ phases. The experimental data points correspond to the pure α-V_2O_5, intercalated $Mg_{0.2}V_2O_5$ and pure δ-$Mg_1V_2O_5$.

both the α (blue) and δ (red) phases. In other layered materials, van der Waals interactions are known to cause layer binding in the deintercalated limit,[59] which is not well described by standard DFT calculations.[60,61] Therefore, in order to obtain a better estimate of the layer spacing values, additional calculations are performed using the vdW-DF2 functional,[62,63] which includes the van der Waals interactions, in addition to the Hubbard +U Hamiltonian (for removing self-interaction errors).

The layer spacing values in Figure 3 are taken from the relaxed ground states for α and δ in Figure 2a. The blue circles and red squares are obtained from PBE (+U) calculations, while the blue and red triangles are calculated with vdW-DF2 (+U). The experimental values listed (green diamonds) correspond to pure α-V_2O_5,[8] $Mg_{0.2}V_2O_5$ (reported by Pereira-Ramos et al.[22]), and pure δ-$Mg_1V_2O_5$.[64] As expected, the PBE and vdW-DF2 layer spacing values differ at complete

DOI: 10.1021/acs.chemmater.5b00957
Chem. Mater. 2015, 27, 3733−3742

demagnesiation (~0.3 Å) but remain similar at all other Mg concentrations, where the layer spacing is determined by the electrostatics and short-range repulsion.

With increasing Mg concentration, the layer spacing increases significantly for α-V_2O_5 (~9% increase from x_{Mg} = 0 to x_{Mg} = 0.5 while using vdW-DF2) but remains fairly constant in δ-V_2O_5 (~2% increase from x_{Mg} = 0 to x_{Mg} = 1). However, the layer spacing in the δ phase remains higher than in the α phase across all Mg concentrations. Also, the layer spacing seen in the α phase (with vdW-DF2) benchmarks better with experimental layer spacing values at low Mg concentrations (up to x_{Mg} = 0.2), compared to the δ phase. Although including the van der Waals corrections in DFT leads to better agreement with the experimental V_2O_5 layer spacing, the Mg insertion voltage is overestimated[30] (by 18%, compared to 6% with PBE+U), showing that PBE+U describes the energetics more accurately than vdW-DF2. If the $Mg_xV_2O_5$ hull (Figure 2a) were to be calculated with vdW-DF2, we speculate that the energies of the demagnesiated structures will shift to higher values than PBE+U, since van der Waals corrections have a tendency to penalize under-bound (demagnesiated) structures.

4.3. Mg Diffusion Barriers in V_2O_5. To gain insight into the migration behavior of Mg in α and δ polymorphs, the calculated activation barriers using the NEB method are plotted in Figure 4. The migration energy is plotted along the diffusion path with the energies of the end points referenced to zero and the total path distance normalized to 100%. The diffusion paths in both α and δ polymorphs correspond to the shortest Mg hop along the a-direction as in Figure 1a and 1b respectively and perpendicular to the b–c plane in Figure 1c. The energy difference between the site with the highest energy along the path (the activated state) and the end points is the migration barrier. A simple random walk model for diffusion would predict that an increase in the activation barrier of ~60 meV would cause a drop in diffusivity by ~1 order of magnitude at 298 K.

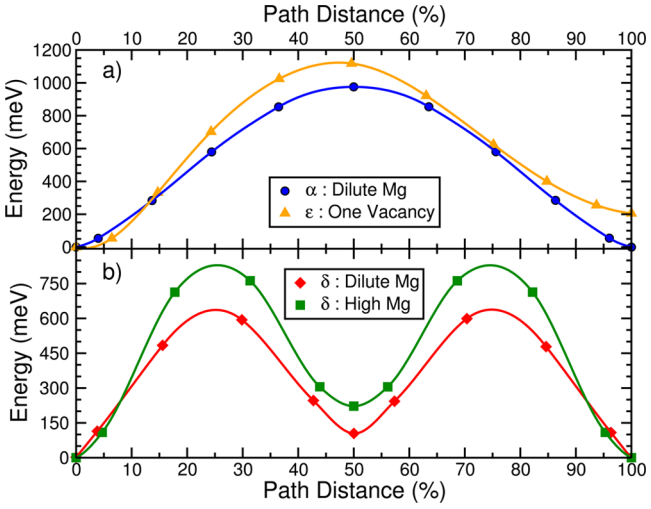

Figure 4. (a) Activation barriers for Mg diffusion in select limiting cases in α-V_2O_5 and (b) for Mg diffusion in δ-V_2O_5 calculated through the NEB method.

Specifically, we have performed four sets of calculations: dilute Mg concentration (x_{Mg} = 0.08) in the α phase (blue dots in Figure 4a), high Mg concentration (x_{Mg} = 0.44) in the α phase (orange triangles), dilute Mg concentration (x_{Mg} = 0.08) in the δ phase (red diamonds in Figure 4b) and high Mg concentrations (x_{Mg} = 0.92) in the δ phase (green squares). Because of the mechanical instability of the α phase at high Mg concentrations, we performed NEB calculations in the ϵ phase. Because the ϵ phase has a specific Mg ordering, migration to an equivalent site requires two symmetrically equivalent hops. Therefore, the path in the orange triangles of Figure 4a only shows one-half of the total path.

The data in Figure 4 illustrates that the barriers in the δ phase (~600–760 meV) are consistently much lower than in the α-phase (~975–1120 meV), with the respective migration energies adopting "valley" and "plateau" shapes. Upon addition of Mg the migration barriers in α and δ both increase. The differences in the magnitude of the migration barriers and the shape of the migration energies between the α and δ can be explained by considering the changes in the coordination environment of Mg along the diffusion path. For example, in the α phase, Mg migrates between adjacent 8-fold coordinated sites through a shared 3-fold coordinated site (activated state), a net 8 → 3 → 8 coordination change, while in the δ phase Mg migrates between adjacent 6-fold coordinated sites through two 3-fold coordinated sites separated by a metastable 5-fold coordinated "valley", a net 6 → 3 → 5 → 3 → 6 coordination change. Hence, the lower barriers of the δ phase, compared to the α phase, are likely due to the smaller coordination changes and the higher layer spacing in δ than α, as seen in Figure 3. The indication of superior diffusivity of Mg in δ-V_2O_5 motivates investigating the intercalation properties of Mg in the δ phase further.

4.4. Cluster Expansion on Mg in δ-V_2O_5 and Temperature–Composition Phase Diagram. Consistent with the data in Figure 2a, all Mg-Va arrangements have higher energy than the linear combination of δ-V_2O_5 and δ-MgV_2O_5, supporting phase separation on the δ lattice as illustrated in Figure 5a, where the zero on the energy scale is referenced to the DFT calculated end members of the δ phase. A total of 97 Mg-Va configurations, across Mg concentrations, are used to construct the CE, which encompasses 13 clusters with a RMSE

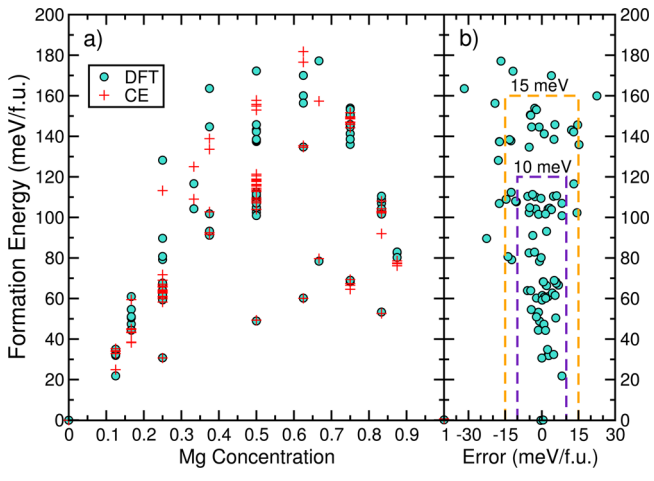

Figure 5. (a) DFT and cluster expansion predicted formation energies are plotted on the vertical scale, with respect to different Mg concentrations on the horizontal scale. (b) Staircase plot indicating the errors in energies encountered for structures using the cluster expansion (horizontal scale), with respect to their respective distances from the hull (vertical scale).

DOI: 10.1021/acs.chemmater.5b00957
Chem. Mater. 2015, 27, 3733–3742

of ∼9 meV/f.u. The CE's weighted cross validation (WCV) score of ∼12.25 meV/f.u. indicates a very good match with the current input set and good predictive capability. In Figure 5b, the staircase plot displays the error in predicting the formation energies of different Mg-Va configurations by the CE against their respective DFT formation energies. A good CE will have lower errors for configurations that are closer to the hull, i.e., shorter absolute distance from the ground state hull, and higher errors for configurations that are further away from the hull. The current CE displays errors below 10 meV/f.u. for most structures whose formation energies are smaller than 120 meV/f.u. Also, it can be seen in Figure 5b that the structures with the highest errors in the formation energy prediction normally have formation energies greater than 125 meV/f.u.

The ECIs for the clusters in the CE, normalized by their multiplicity and plotted against their respective cluster sizes, are displayed in Figure 6. The size of a given cluster is indicated by its longest dimension; for example, in a triplet, the cluster size is given by its longest pair. Negative pair terms indicate "attraction" (i.e., Mg-Mg and Va-Va pairs are favored) and positive pair terms indicate "repulsion" (i.e., Mg-Va pairs are favored). The figures inside the graph show the triplets and the quadruplet used in the current CE with the solid lines indicating interactions in the $a-b$ plane and dotted lines indicating interactions out of plane (b is the direction perpendicular to the V_2O_5 layers). The orange circles indicate Mg atoms. The data in Figure 6 illustrate that the most dominant (highest absolute ECI value) cluster of the CE is a triplet, where Mg ions are along the $a-b$ plane (as shown in Figure 1b). The most dominant pair term is attractive and is the longest pair of the most dominant triplet. The negative sign of the dominant triplet and the dominant pair terms implies that there are two possible configurations containing Mg that are stabilized: (i) all three sites are occupied by Mg, and (ii) only one of the three sites is occupied by Mg, consistent with the sign convention adopted in the CE ($\sigma_i = 1$ for occupied Mg site and $\sigma_i = -1$ for a vacancy).

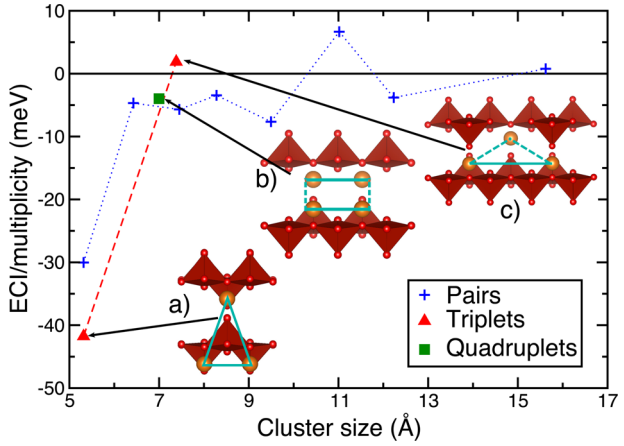

Figure 6. Plot of ECI of the clusters versus their respective cluster size. Insets (a) and (c) display the triplet terms, and inset (b) shows the quadruplet term with the solid blue lines indicating in-plane interactions and the dotted blue lines indicating out-of-plane interactions. All insets are displayed on the $a-b$ plane.

The temperature−concentration phase diagram for Mg intercalation into δ-V_2O_5 is displayed in Figure 7. The black line traces the phase boundary between the single-phase and two-phase regions, obtained from Monte Carlo simulations with the numerical hysteresis removed by free-energy integration. Consistent with the δ hull in Figure 2a, the Mg−V_2O_5 is a phase-separating system at room temperature with extremely low solubilities at either ends (<1%). Note that only the solid δ-phase is considered in this phase diagram. In reality, the high-temperature part of the phase diagram would probably form a eutectic since pure V_2O_5 melts at ∼954 K.[65]

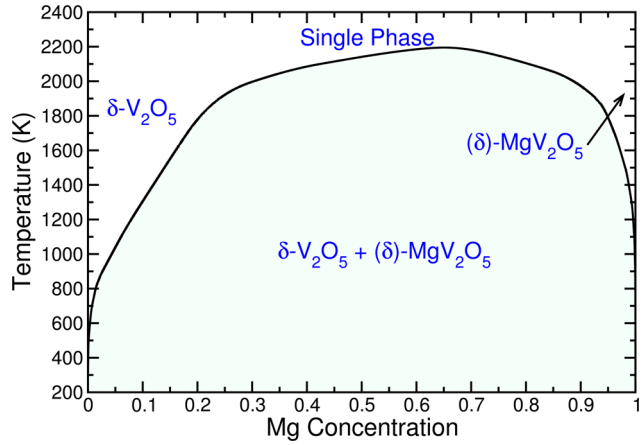

Figure 7. Mg−V_2O_5 intercalation phase diagram for the δ phase. The black line indicates the phase boundary between the single-phase and two-phase regions obtained from Monte Carlo simulations of the CE.

5. DISCUSSION

In this work, we have performed a first-principles investigation of Mg intercalation into orthorhombic V_2O_5. Specifically, we investigated the α and δ polymorphs using DFT calculations, evaluating their respective ground-state hulls, subsequent voltage curves, and their Mg migration barriers. For the δ polymorph, we constructed the composition−temperature phase diagram using the CE and GMC approach. The theoretical data that we have collected not only shed light on the existing experiments intercalating Mg into V_2O_5, but also provide a practical strategy to improve performance.

From a thorough comparison of the experimental data available in the literature to the calculations performed in this work, we conclude that by synthesizing V_2O_5 and intercalating Mg (i.e., beginning in the charged state), the structure remains in the α phase. For example, in the experimental voltage curves,[13,22,25−27] the characteristic plateau followed by a drop at $x_{Mg} \approx 0.5$ compares well with the computed voltage curve for the α phase (Figure 2b), which shows a similar voltage drop, corresponding to the ϵ ordering, while δ-V_2O_5 would show no such drop. With regard to X-ray diffraction (XRD) data, in the literature on magnesiated V_2O_5, no additional peaks have been observed, which would indicate the formation of the δ phase.[22,25,66] Also, the observed increase in the layer spacing[25] is consistent with the computed predictions of layer expansion in the α phase until $x_{Mg} = 0.5$ (Figure 3) rather than the δ phase, which has a minimal increase in layer spacing from $x_{Mg} = 0$ to $x_{Mg} = 1$. The migration barriers for Mg in the α phase are high (∼975 meV as seen in Figure 4a), and indeed, reversible Mg insertion can be reliably achieved only when the diffusion length is greatly reduced (i.e., in thin films and nanopowders) and at very low rates (i.e., ∼0.5 μA/cm^2 by Gershinsky et al.[25]). Magnesiation past the ϵ-phase ($x_{Mg} \approx 0.5$) is expected to be

DOI: 10.1021/acs.chemmater.5b00957
Chem. Mater. 2015, 27, 3733−3742

difficult as the potential drops, thereby reducing the driving force for Mg insertion, and the Mg migration barrier increases with Mg concentration in α (Figure 4a). While the driving force to transform from $\alpha \rightarrow \delta$ is small up to $x_{Mg} \approx 0.5$ (as in Figure 2a), it steeply increases thereafter, leading us to speculate that further magnesiation would lead to the formation of a fully magnesiated δ-MgV_2O_5 on the surface.

Our thinking on the magnesiation process of V_2O_5 is summarized in Figure 8. The ground-state hull in Figure 2a

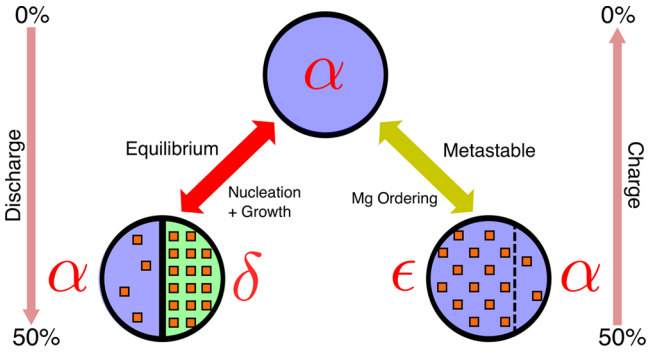

Figure 8. Possible intercalation pathways for Mg in V_2O_5 up to x_{Mg} = 0.5. The left half corresponds to the equilibrium case where the δ phase nucleates and grows in a supersaturated α phase, with a well-defined interface between the two phases, and the right half corresponds to the Mg atoms ordering into the metastable ϵ phase and the lack of a well-defined interface in this case, since ϵ and α have the same V_2O_5 layer stacking.

suggests that, under equilibrium conditions, the Mg insertion mechanism is through a two-phase reaction, by nucleation and growth of magnesiated δ phase from supersaturated α, rather than through the metastable formation of the ϵ phase. These two reaction pathways (cycling between 0 and 50% state of charge) are illustrated schematically in Figure 8, with the orange squares representing Mg atoms. If nucleation and growth of the fully magnesiated δ phase (i.e., x_{Mg} = 1) were to occur, there would be no inherent upper limit to magnesium insertion up to $x_{Mg} \approx 1$. However, the metastable insertion path of Mg in the α phase, which, once fully converted to ϵ phase, remains at $x_{Mg} \approx 0.5$, is more consistent with experiments. The reason the system follows the metastable insertion path through α is that the equilibrium path (α-V_2O_5 to δ-MgV_2O_5) requires structural rearrangement of the host structure through the translation of V_2O_5 layers, which may be difficult kinetically once some Mg is inserted and more strongly bonds the layers. Also, a nucleation−growth process involves high interfacial energies and may lead to low rates. A similar metastable solid solution transformation has been predicted and documented for other thermodynamic phase-separating systems.[67−69]

While our calculations, supported by experimental data, suggest that the host V_2O_5 structure remains in the α phase upon Mg intercalation, they also suggest an approach to substantially improve the electrochemical properties by cycling Mg beginning in the δ phase. Mg in δ-V_2O_5 not only possesses a higher average voltage compared to α (~120 mV higher as seen in Figure 2b), but also a significantly better mobility (~600−760 meV, compared to ~975−1120 meV), which accounts for ~5 orders of magnitude improvement in the diffusivity at room temperature (Figure 4). Prior computations have reported higher migration barriers in the δ phase, compared to the α phase in the charged limit, in contrast to our calculations in Figure 4,[31] which we attribute to the authors allowing only Mg and nearby O ions to relax in their NEB calculations. In order to cycle Mg in the δ phase, V_2O_5 must be prepared in the fully discharged state (δ-$Mg_1V_2O_5$), where the δ phase is thermodynamically stable. Fortunately, the synthesis of δ-MgV_2O_5 is well-established in the literature.[64]

Since, at intermediate Mg concentrations, the equilibrium state is a coexistence between the demagnesiated α-phase and the fully magnesiated δ-phase, the δ phase must remain metastable over a wide Mg concentration range to ensure higher capacities. If the δ-phase is not metastable, transformation to the α-phase will take place. We speculate that the possibility of δ phase metastability is likely, given that nucleation and growth of the α phase requires restructuring of the host lattice, and the absence of mechanically unstable Mg configurations (even at x_{Mg} = 0) in δ (Figure 2a) in our calculations. Also, an applied (over)underpotential is required to access a metastable (de)insertion path, which can be quantified by the difference between the metastable and equilibrium voltage curves in Figure 2b. For example, to avoid the equilibrium path, an applied underpotential of ~800 mV is required to insert Mg and retain the α-V_2O_5 structure, but only ~400 mV is required to remove Mg and retain the δ-MgV_2O_5 structure, which supports the possibility of a metastable δ phase.

Assuming the δ-MgV_2O_5 phase remains metastable, the temperature−composition phase diagram computed for Mg in δ-V_2O_5 using the CE (Figure 7) indicates a phase-separating behavior with negligible solubility at both end members at room temperature. By investigating the dominant interactions (ECIs) that contribute to the CE, we gain some insight into the possible intercalation mechanism. The dominant Mg-Va interactions, specifically the triplet and the nearest interlayer pair as seen in Figure 6, are entirely contained in the a−b plane, which indicates that the δ-V_2O_5 host lattice will contain fully magnesiated and fully demagnesiated domains separated by an interface along an a−b plane. Hence, Mg insertion into the three-dimensional (3D) δ-V_2O_5 structure can be effectively described by considering the interactions in each two-dimensional (2D) a−b plane.

Figure 9 illustrates the interplay between these dominant pair and triplet terms, which results in the specific sequence of Mg-Va configurations in terms of their relative stability. The orange circles indicate Mg atoms, the hollow circles the vacancies, and all insets are viewed in the a−b plane. Given the sign convention used in the CE (σ_i = 1 for Mg and σ_i = −1 for Va) and the negative sign of the dominant pair and triplet, the formation of Mg−Mg and Va-Va pairs are favored while triplets containing one or three Mg atoms are favored. Thus, a fully occupied triplet is most stable due to favorable contributions from both the triplet (approximately −40 meV) and the two longest pair terms (approximately −60 meV in total) resulting in a net stabilization of approximately −100 meV, while the triplet with two Mg atoms forming the shortest pair and a vacancy at the apex is least stable, because of unfavorable contributions from both the pairs and the triplet, resulting in a destabilizing contribution of approximately +100 meV.

The bottom half of Figure 9 illustrates a sample sequence in which Mg atoms fill up sites on a given a−b plane. The fully magnesiated structure (right inset) is highly stabilized due to the presence of fully filled triplets (approximately −100 meV/triplet) while the fully demagnesiated structure (right inset) is stabilized to a lesser extent (approximately −20 meV/triplet).

DOI: 10.1021/acs.chemmater.5b00957
Chem. Mater. 2015, 27, 3733−3742

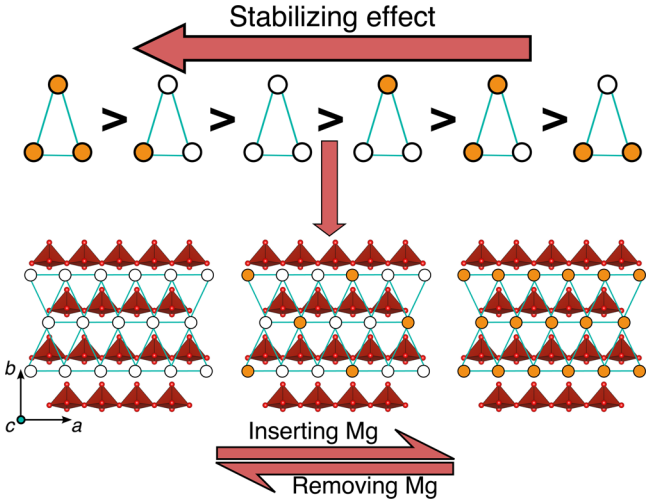

Figure 9. Interplay between the dominant pair and triplet terms of the CE stabilizing different Mg-Va arrangements.

At an intermediate composition, the Mg atoms will arrange themselves in such a way that the number of fully filled and one-third-filled triplets (approximately −40 meV/triplet, depicted in the center inset) is maximized. Since one-third-filled triplets stabilize a structure more than triplets containing two Mg atoms, non-phase-separated configurations at low Mg concentrations ($x_{Mg} < 0.33$) will be more stabilized than those at high Mg concentrations ($x_{Mg} > 0.66$), as indicated by the higher solubilities at lower Mg concentrations in the phase diagram shown in Figure 7 at high temperatures.

Since the occurrence of fully magnesiated and demagnesiated $a-b$ planes is highly stabilized, the intercalation of Mg in the 3D δ-V_2O_5 structure will then progress via propagation of fully magnesiated $a-b$ planes along the c-axis. With additional applied overpotential, not only can the δ phase be retained, but also a nonequilibrium solid solution intercalation pathway in δ can be thermodynamically accessible, leading to further improved kinetics.[67] An estimate for the additional overpotential required can be computed by considering the lowest energy structure at $x_{Mg} = 0.83$ in Figure 5a, whose formation energy is 53 meV/Mg, resulting in an approximate additional overpotential requirement of ∼320 mV. Therefore, the net overpotential required to access a solid-solution transformation path entirely in the δ phase upon charge is ∼720 mV, which is comparable to the underpotential applied (∼800 mV) to remain in the metastable α phase upon discharge. Hence, we suggest that the electrochemical performance of Mg in V_2O_5 can be improved by beginning cycling in the discharged state, δ-MgV_2O_5, with the prospect of improved voltage, capacity, and kinetics.

6. CONCLUSIONS

In this work, we have used first-principles calculations to perform an in-depth investigation of Mg intercalation in the orthorhombic α and δ polymorphs of V_2O_5 to evaluate their suitability as high-energy-density cathode materials for Mg-ion batteries. Specifically, we computed the ground state hulls and the activation energies for Mg migration in both polymorphs. For the δ polymorph, we calculated the temperature−composition phase diagram. The equilibrium state of $Mg_xV_2O_5$ ($0 < x_{Mg} < 1$) is determined to be a two-phase coexistence between the fully magnesiated δ-MgV_2O_5 and fully demagnesiated α-V_2O_5 phases. NEB calculations indicate that room-temperature Mg migration is several orders of magnitude faster in the δ phase ($E_m \approx 600-760$ meV) than in the α phase ($E_m \approx 975-1120$ meV).

By comparing the calculated voltage curves and changes in the layer spacing with intercalation with available experimental data on Mg insertion in V_2O_5, we conclude that the α phase likely remains metastable when Mg is initially inserted into fully demagnesiated α-V_2O_5. Although the computed α phase migration barriers indicate poor Mg mobility, consistent with reversible Mg intercalation being achievable exclusively at very low rates and in small particles, α-V_2O_5 is still one of only three known cathode materials where reversible cycling of Mg is possible at all (along with chevrel Mo_6S_8 and layered MoO_3).

Therefore, our finding that the δ-V_2O_5 polymorph displays vastly superior Mg mobility, as well as a modest increase in voltage, compared to the α phase is especially promising, assuming that the δ-V_2O_5 host structure can remain stable or metastable across a wide Mg concentration range. Fortunately, the δ polymorph is thermodynamically stable in the fully discharged state and its synthesis procedure well-known.

From our first-principles calculations of the formation energies of several Mg orderings in the δ-V_2O_5 host structure and the resulting computed temperature−composition phase diagram, we have also gained insight into the possible mechanism of Mg intercalation within the δ host structure. At room temperature, Mg displays strong phase-separating behavior with negligible solid-solution in the end-member phases and favors the formation of either completely full or empty $a-b$ planes, which are perpendicular to the layers formed by the connecting VO_5 pyramids, suggesting an intercalation mechanism based on nucleation and growth through the propagation of an $a-b$ interface along the c-axis.

AUTHOR INFORMATION

Corresponding Author

*Tel.: +1 617 253 1581. Fax: +1 617 253 1581. E-mail: gceder@mit.edu.

Notes

The authors declare no competing financial interest.

ACKNOWLEDGMENTS

The current work is fully supported by the Joint Center for Energy Storage Research (JCESR), an Energy Innovation Hub funded by the U.S. Department of Energy, Office of Science and Basic Energy Sciences. This study was supported by Subcontract No. 3F-31144. The authors thank the National Energy Research Scientific Computing Center (NERSC) for providing computing resources. S.G. would like to thank William D. Richards at MIT for fruitful feedback and suggestions.

REFERENCES

(1) Noorden, R. V. The rechargeable revolution: A better battery. *Nature* **2014**, *507*, 26−28.

(2) Shterenberg, I.; Salama, M.; Gofer, Y.; Levi, E.; Aurbach, D. The challenge of developing rechargeable magnesium batteries. *MRS Bull.* **2014**, *39*, 453−460.

(3) Aurbach, D.; Lu, Z.; Schechter, A.; Gofer, Y.; Gizbar, H.; Turgeman, R.; Cohen, Y.; Moshkovich, M.; Levi, E. Prototype systems for rechargeable magnesium batteries. *Nature* **2000**, *407*, 724−727.

DOI: 10.1021/acs.chemmater.5b00957
Chem. Mater. 2015, 27, 3733−3742

(4) Yoo, H. D.; Shterenberg, I.; Gofer, Y.; Gershinsky, G.; Pour, N.; Aurbach, D. Mg rechargeable batteries: an on-going challenge. *Energy Environ. Sci.* **2013**, *6*, 2265−2279.
(5) Jain, A.; Ong, S. P.; Hautier, G.; Chen, W.; Richards, W. D.; Dacek, S.; Cholia, S.; Gunter, D.; Skinner, D.; Ceder, G.; Persson, K. A. Commentary: The Materials Project: A materials genome approach to accelerating materials innovation. *APL Mater.* **2013**, *1*, 011002.
(6) Whittingham, M. S. Lithium batteries and cathode materials. *Chem. Rev.* **2004**, *104*, 4271−4301.
(7) Bachmann, H. G.; Ahmed, F. R.; Barnes, W. H. The crystal structure of vanadium pentoxide. *Z. Kristallogr.* **1961**, *115*, 110−131.
(8) Enjalbert, R.; Galy, J. A refinement of the structure of V_2O_5. *Acta Crystallogr., Sect. C* **1986**, *42*, 1467−1469.
(9) Millet, P.; Satto, C.; Bonvoisin, J.; Normand, B.; Penc, K.; Albrecht, M.; Mila, F. Magnetic properties of the coupled ladder system MgV_2O_5. *Phys. Rev. B* **1998**, *57*, 5005−5008.
(10) Korotin, M. A.; Anisimov, V. I.; Saha-Dasgupta, T.; Dasgupta, I. Electronic structure and exchange interactions of the ladder vanadates CaV_2O_5 and MgV_2O_5. *J. Phys.: Condens. Matter* **2000**, *12*, 113−124.
(11) Whittingham, M. S. The Role of Ternary Phases in Cathode Reactions. *J. Electrochem. Soc.* **1976**, *123*, 315−320.
(12) Galy, J.; Hardy, A. Structure cristalline du bronze de vanadium-lithium LiV_2O_5. *Acta Crystallogr.* **1965**, *19*, 432−435.
(13) Amatucci, G. G.; Badway, F.; Singhal, A.; Beaudoin, B.; Skandan, G.; Bowmer, T.; Plitz, I.; Pereira, N.; Chapman, T.; Jaworski, R. Investigation of Yttrium and Polyvalent Ion Intercalation into Nanocrystalline Vanadium Oxide. *J. Electrochem. Soc.* **2001**, *148*, A940−A950.
(14) Delmas, C.; Cognac-Auradou, H.; Cocciantelli, J. M.; Ménétrier, M.; Doumerc, J. P. The $Li_xV_2O_5$ system: An overview of the structure modifications induced by the lithium intercalation. *Solid State Ionics* **1994**, *69*, 257−264.
(15) Murphy, D. W.; Christian, P. A.; DiSalvo, F. J.; Waszczak, J. V. Lithium incorporation by vanadium pentoxide. *Inorg. Chem.* **1979**, *18*, 2800−2803.
(16) Dickens, P. G.; French, S. J.; Hight, A. T.; Pye, M. F.; Reynolds, G. J. Thermochemistry of the high and ambient temperature lithium vanadium bronze phases $Li_xV_2O_5$. *Solid State Ionics* **1981**, *2*, 27−32.
(17) Wiesener, K.; Schneider, W.; Ilić, D.; Steger, E.; Hallmeier, K.; Brackmann, E. Vanadium oxides in electrodes for rechargeable lithium cells. *J. Power Sources* **1987**, *20*, 157−164.
(18) Wu, Q.-H.; Thißen, A.; Jaegermann, W. Photoelectron spectroscopic study of Li intercalation into V_2O_5 thin films. *Surf. Sci.* **2005**, *578*, 203−212.
(19) Braithwaite, J. S.; Catlow, C. R. A.; Gale, J. D.; Harding, J. H. Lithium Intercalation into Vanadium Pentoxide: A Theoretical Study. *Chem. Mater.* **1999**, *11*, 1990−1998.
(20) Rocquefelte, X.; Boucher, F.; Gressier, P.; Ouvrard, G. First-Principle Study of the Intercalation Process in the $Li_xV_2O_5$ System. *Chem. Mater.* **2003**, *15*, 1812−1819.
(21) Scanlon, D. O.; Walsh, A.; Morgan, B. J.; Watson, G. W. An ab initio Study of Reduction of V_2O_5 through the Formation of Oxygen Vacancies and Li Intercalation. *J. Phys. Chem. C* **2008**, *112*, 9903−9911.
(22) Pereira-Ramos, J.; Messina, R.; Perichon, J. Electrochemical formation of a magnesium vanadium bronze $Mg_xV_2O_5$ in sulfone-based electrolytes at 150 °C. *J. Electroanal. Chem.* **1987**, *218*, 241−249.
(23) Gregory, T. D.; Hoffman, R. J.; Winterton, R. C. Nonaqueous Electrochemistry of Magnesium. *J. Electrochem. Soc.* **1990**, *137*, 775−780.
(24) Novák, P.; Imhof, R.; Haas, O. Magnesium insertion electrodes for rechargeable nonaqueous batteries a competitive alternative to lithium? *Electrochim. Acta* **1999**, *45*, 351−367.
(25) Gershinsky, G.; Yoo, H. D.; Gofer, Y.; Aurbach, D. Electrochemical and spectroscopic analysis of Mg^{2+} intercalation into thin film electrodes of layered oxides: V_2O_5 and MoO_3. *Langmuir* **2013**, *29*, 10964−10972.
(26) Novak, P.; Desilvestro, J. Electrochemical Insertion of Magnesium in Metal Oxides and Sulfides from Aprotic Electrolytes. *J. Electrochem. Soc.* **1993**, *140*, 140−144.
(27) Yu, L.; Zhang, X. Electrochemical insertion of magnesium ions into V_2O_5 from aprotic electrolytes with varied water content. *J. Colloid Interface Sci.* **2004**, *278*, 160−165.
(28) Shklover, V.; Haibach, T.; Ried, F.; Nesper, R.; Novák, P. Crystal Structure of the Product of Mg^{2+} Insertion into V_2O_5 Single Crystals. *J. Solid State Chem.* **1996**, *123*, 317−323.
(29) Wang, Z.; Su, Q.; Deng, H. Single-layered V_2O_5: A promising cathode material for rechargeable Li and Mg ion batteries: An ab initio study. *Phys. Chem. Chem. Phys.* **2013**, *15*, 8705−8709.
(30) Carrasco, J. Role of van der Waals Forces in Thermodynamics and Kinetics of Layered Transition Metal Oxide Electrodes: Alkali and Alkaline-Earth Ion Insertion into V_2O_5. *J. Phys. Chem. C* **2014**, *118*, 19599−19607.
(31) Zhou, B.; Shi, H.; Cao, R.; Zhang, X.; Jiang, Z. Theoretical study on the initial stage of Magnesium battery based on V_2O_5 cathode. *Phys. Chem. Chem. Phys.* **2014**, *16*, 18578−18585.
(32) Ceder, G.; Van der Ven, A. Phase diagrams of lithium transition metal oxides: Investigations from first principles. *Electrochim. Acta* **1999**, *45*, 131−150.
(33) Zhou, F.; Maxisch, T.; Ceder, G. Configurational Electronic Entropy and the Phase Diagram of Mixed-Valence Oxides: The Case of Li_xFePO_4. *Phys. Rev. Lett.* **2006**, *97*, 155704.
(34) Ceder, G. A derivation of the Ising model for the computation of phase diagrams. *Comput. Mater. Sci.* **1993**, *1*, 144−150.
(35) Bouloux, J.-C.; Milosevic, I.; Galy, J. Les hypovanadates de magnésium $MgVO_3$ et MgV_2O_5. Structure cristalline de $MgVO_3$. *J. Solid State Chem.* **1976**, *16*, 393−398.
(36) Cocciantelli, J.; Doumerc, J.; Pouchard, M.; Broussely, M.; Labat, J. Crystal chemistry of electrochemically inserted $Li_xV_2O_5$. *J. Power Sources* **1991**, *34*, 103−111.
(37) Cava, R.; Santoro, A.; Murphy, D.; Zahurak, S.; Fleming, R.; Marsh, P.; Roth, R. The structure of the lithium-inserted metal oxide δLiV_2O_5. *J. Solid State Chem.* **1986**, *65*, 63−71.
(38) Kohn, W.; Sham, L. J. Self-Consistent Equations Including Exchange and Correlation Effects. *Phys. Rev.* **1965**, *140*, A1133−A1138.
(39) Kresse, G.; Hafner, J. Ab initio molecular dynamics for liquid metals. *Phys. Rev. B* **1993**, *47*, 558−561.
(40) Kresse, G.; Furthmüller, J. Efficient iterative schemes for ab initio total-energy calculations using a plane-wave basis set. *Phys. Rev. B* **1996**, *54*, 11169−11186.
(41) Perdew, J. P.; Burke, K.; Ernzerhof, M. Generalized Gradient Approximation Made Simple. *Phys. Rev. Lett.* **1996**, *77*, 3865−3868.
(42) Kresse, G.; Joubert, D. From ultrasoft pseudopotentials to the projector augmented-wave method. *Phys. Rev. B* **1999**, *59*, 1758−1775.
(43) Anisimov, V. I.; Zaanen, J.; Andersen, O. K. Band theory and Mott insulators: Hubbard U instead of Stoner I. *Phys. Rev. B* **1991**, *44*, 943−954.
(44) Zhou, F.; Cococcioni, M.; Marianetti, C.; Morgan, D.; Ceder, G. First-principles prediction of redox potentials in transition-metal compounds with LDA+U. *Phys. Rev. B* **2004**, *70*, 235121.
(45) Jain, A.; Hautier, G.; Ong, S. P.; Moore, C. J.; Fischer, C. C.; Persson, K. A.; Ceder, G. Formation enthalpies by mixing GGA and GGA + U calculations. *Phys. Rev. B* **2011**, *84*, 045115.
(46) Sanchez, J.; Ducastelle, F.; Gratias, D. Generalized cluster description of multicomponent systems. *Physica A* **1984**, *128*, 334−350.
(47) Van der Ven, A.; Marianetti, C.; Morgan, D.; Ceder, G. Phase transformations and volume changes in spinel $Li_xMn_2O_4$. *Solid State Ionics* **2000**, *135*, 21−32.
(48) Ong, S. P.; Richards, W. D.; Jain, A.; Hautier, G.; Kocher, M.; Cholia, S.; Gunter, D.; Chevrier, V. L.; Persson, K. A.; Ceder, G. Python Materials Genomics (pymatgen): A robust, open-source python library for materials analysis. *Comput. Mater. Sci.* **2013**, *68*, 314−319.

DOI: 10.1021/acs.chemmater.5b00957
Chem. Mater. 2015, 27, 3733−3742

(49) Hart, G.; Forcade, R. Algorithm for generating derivative structures. *Phys. Rev. B* **2008**, *77*, 224115.
(50) Hart, G.; Forcade, R. Generating derivative structures from multilattices: Algorithm and application to hcp alloys. *Phys. Rev. B* **2009**, *80*, 014120.
(51) Hart, G. L.; Nelson, L. J.; Forcade, R. W. Generating derivative structures at a fixed concentration. *Comput. Mater. Sci.* **2012**, *59*, 101−107.
(52) Nelson, L.; Hart, G.; Zhou, F.; Ozoliš, V. Compressive sensing as a paradigm for building physics models. *Phys. Rev. B* **2013**, *87*, 035125.
(53) Goldstein, T.; Osher, S. The Split Bregman Method for L1-Regularized Problems. *SIAM J. Imag. Sci.* **2009**, *2*, 323−343.
(54) Walle, A.; Ceder, G. Automating first-principles phase diagram calculations. *J. Phase Equilib.* **2002**, *23*, 348−359.
(55) Van der Ven, A.; Thomas, J.; Xu, Q.; Bhattacharya, J. Linking the electronic structure of solids to their thermodynamic and kinetic properties. *Math. Comput. Simul.* **2010**, *80*, 1393−1410.
(56) Hinuma, Y.; Meng, Y.; Ceder, G. Temperature-concentration phase diagram of $P_2Na_xCoO_2$ from first-principles calculations. *Phys. Rev. B* **2008**, *77*, 224111.
(57) Sheppard, D.; Terrell, R.; Henkelman, G. Optimization methods for finding minimum energy paths. *J. Chem. Phys.* **2008**, *128*, 134106.
(58) Liu, M.; Rong, Z.; Malik, R.; Canepa, P.; Jain, A.; Ceder, G.; Persson, K. A. Spinel compounds as multivalent battery cathodes: A systematic evaluation based on ab initio calculations. *Energy Environ. Sci.* **2015**, *8*, 964−974.
(59) Amatucci, G. G.; Tarascon, J.; Klein, L. CoO_2, The End Member of the Li_xCoO_2 Solid Solution. *J. Electrochem. Soc.* **1996**, *143*, 1114−1123.
(60) French, R. H.; et al. Long range interactions in nanoscale science. *Rev. Mod. Phys.* **2010**, *82*, 1887−1944.
(61) Rydberg, H.; Dion, M.; Jacobson, N.; Schröder, E.; Hyldgaard, P.; Simak, S.; Langreth, D.; Lundqvist, B. Van der Waals Density Functional for Layered Structures. *Phys. Rev. Lett.* **2003**, *91*, 126402.
(62) Lee, K.; Murray, E. D.; Kong, L.; Lundqvist, B. I.; Langreth, D. C. A Higher-Accuracy van der Waals Density Functional. *Phys. Rev. B* **2010**, *82*, 081101(R).
(63) Klime, J.; Bowler, D. R.; Michaelides, A. Van der Waals density functionals applied to solids. *Phys. Rev. B* **2011**, *83*, 195131.
(64) Millet, P.; Satto, C.; Sciau, P.; Galy, J. A Comparative Structural Investigation. *J. Solid State Chem.* **1998**, *62*, 56−62.
(65) Haynes, W. M. *CRC Handbook of Chemistry and Physics*, 95th Edition; CRC Press: Boca Raton, FL, 2014.
(66) Novák, P.; Shklover, V.; Nesper, R. Magnesium Insertion in Vanadium Oxides: A Structural Study. *Z. Phys. Chem.* **1994**, *185*, 51−68.
(67) Malik, R.; Zhou, F.; Ceder, G. Kinetics of non-equilibrium lithium incorporation in $LiFePO_4$. *Nat. Mater.* **2011**, *10*, 587−590.
(68) Kang, S.; Mo, Y.; Ong, S. P.; Ceder, G. A facile mechanism for recharging Li_2O_2 in LiO_2 batteries. *Chem. Mater.* **2013**, *25*, 3328−3336.
(69) Ganapathy, S.; Adams, B. D.; Stenou, G.; Anastasaki, M. S.; Goubitz, K.; Miao, X.-F.; Nazar, L. F.; Wagemaker, M. Nature of Li_2O_2 Oxidation in a LiO_2 Battery Revealed by Operando X-ray Diffraction. *J. Am. Chem. Soc.* **2014**, *136*, 16335−16344.

DOI: 10.1021/acs.chemmater.5b00957
Chem. Mater. 2015, 27, 3733−3742